# Fast Photoresponse from 1T Tin Diselenide Atomic Layers

*Peng Yu, Xuechao Yu, Wanglin Lu, Hsin Lin, Linfeng Sun, Kezhao Du, Fucai Liu, Wei Fu, Qingsheng Zeng, Zexiang Shen, Chuanhong Jin, Qi Jie Wang,* and Zheng Liu**

**Atomically layered 2D crystals such as transitional metal dichalcogenides (TMDs) provide an enchanting landscape for optoelectronic applications due to their unique atomic structures. They have been most intensively studied with 2H phase for easy fabrication and manipulation. 1T phase material could possess better electrocatalytic and photocatalytic properties, while they are difficult to fabricate. Herein, for the first time, the atomically layered 1T phase tin diselenides ($SnSe_2$, III-IV compound) are successfully exfoliated by the method of mechanical exfoliation from bulk single crystals, grown via the chemical vapor transport method without transport gas. More attractively, the high performance atomically layered $SnSe_2$ photodetector has been first successfully fabricated, which displays a good responsivity of 0.5 A $W^{-1}$ and a fast photoresponse down to ≈2 ms at room temperature, one of the fastest response times among all types of 2D photodetectors. It makes $SnSe_2$ a promising candidate for high performance optoelectronic devices. Moreover, high performance bilayered $SnSe_2$ field-effect transistors are also demonstrated with a mobility of ≈4 $cm^2 V^{-1} s^{-1}$ and an on/off ratio of $10^3$ at room temperature. The results demonstrate that few layered 1T TMD materials are relatively stable in air and can be exploited for various electrical and optical applications.**

## 1. Introduction

Stimulated by the discovery of graphene and its fascinating electronic and physical properties,[1–4] 2D materials such as hexagonal boron nitride,[5–8] transitional metal dichalcogenides (TMDs),[9–15] and other 2D compounds,[16–18] have received increasing interests because of their great potential in the field of catalysis, nanotribology, microelectronics, lithium batteries, hydrogen storage, medical, and optoelectronics.[19–22] However, their applications in nanoelectronic and optoelectronic devices are limited by the zero bandgap of graphene. The high leaking current in graphene based field-effect transistor (FET) makes it difficult for realization of integrated circuits. For 2D compounds in a form of $MX_2$ (M = transitional and main group metal, X = S, Se, and Te), it typically crystallizes in 2H and 1T types structure with $D_{6h}$ and $D_{3d}$ point-group symmetry, respectively, and the major difference between 2H and 1T is the coordination type of the metal atoms: the trigonal prismatic coordination for the former and the octahedral coordination, in addition, "2" and "1" in 2H and 1T represent the number of the layers in unit cell, shown in Figure S1 (Supporting Information). Substantial efforts have been devoted to study 2H type $MX_2$ 2D crystals (e.g., $MoS_2$, $WSe_2$), because of their stable phase. Potential applications such as valleytronics, ultra-low-power consumption electronics, and high performance catalyst were reported. For example, FETs fabricated using TMD $MX_2$ (M = Mo and W, X = S and Se) atomic layers exhibit excellent on/off current ratio (up to $10^8$) and reasonably good carrier mobility,[22,23] and some $MX_2$ (M = Nb and Ta, X = S and Se) thin films show exciting superconductivity and charge density wave behaviors.[22,24,25]

However, it shed less light on the electronic and optoelectronic properties of 1T-$MX_2$ 2D crystals simply due to the difficulties in synthesis. In addition, the metallic nature of some 1T phase 2D layers makes them not suitable for the fabrications of FET and optoelectronic devices (such as, M = Mo, W, Nb, and Ta, X = S, Se, and Te).[26] 1T-$MX_2$ 2D crystals, however, show several advantages compared with their 2H phase counterparts, e.g., 1T monolayer $WS_2$ displays the better electrocatalytic and photocatalytic properties.[27,28] Therefore, the research of electronic and optoelectronic properties of atomically thin layers of 1T $MX_2$ 2D materials is highly demanding.

Dr. P. Yu, Dr. K. Du, Dr. F. Liu, Dr. W. Fu, Dr. Q. Zeng, Prof. Z. Liu
School of Materials Science and Engineering
Nanyang Technological University
50 Nanyang Avenue, Singapore 639798, Singapore
E-mail: Z.LIU@ntu.edu.sg
X. Yu, Prof. Q. J. Wang
School of Electrical and Electronic Engineering
Nanyang Technological University
50 Nanyang Avenue, Singapore 639798, Singapore
E-mail: qjwang@ntu.edu.sg
W. Lu, Prof, C. Jin
State Key Laboratory of Silicon Materials
School of Materials Science & Engineering
Zhejiang University
Hangzhou, Zhejiang 310027, P. R. China
Prof. H. Lin
Department of Physics
National University of Singapore
Singapore 117542, Singapore
L. Sun, Prof. Z. Shen
School of Physical and Mathematical Sciences
Nanyang Technological University
Singapore 639798, Singapore

DOI: 10.1002/adfm.201503789


© 2015 WILEY-VCH Verlag GmbH & Co. KGaA, Weinheim

Among 1T $MX_2$ 2D crystals, $SnSe_2$ is a semiconductor with bulk bandgap of about 1.0 eV. For a thick $SnSe_2$ film (84 nm) based device, it showed a mobility of 28 $cm^2 V^{-1} s^{-1}$ but a poor on/off ratio in single digit, and a high bulk electron affinity of 5.2 eV according to recent report.[29] In addition, $SnSe_2$ films are also a good candidate for resistive memory and solar cells.[30] However, most of the studies currently focused on thick or bulk $SnSe_2$.[29,31] The properties of atomic layered $SnSe_2$ are still unknown.

In this paper, monolayered and bilayered $SnSe_2$ are first successfully exfoliated via mechanical exfoliation from the single-crystal $SnSe_2$, which have been carefully examined their electronic and optoelectronic behaviors. Complementary characterizing tools such as atomic force microscope (AFM) and Raman microscopy have been employed to characterize the $SnSe_2$ atomic layers. The optoelectronic properties of the bilayer $SnSe_2$ devices were systematically studied, which show a mobility of ≈4 $cm^2 V^{-1} s^{-1}$ and on/off ≈$10^3$. More interestingly, atomic layered $SnSe_2$ exhibits high photoresponsivity reaching 0.5 A $W^{-1}$ and very fast response speed of 2.2 ± 0.3 ms (rise) and 3.2 ± 0.2 ms (fall), exceeding most of other 2D materials like $MoS_2$ and $WSe_2$ layers. These make few-layer $SnSe_2$ a promising active 2D material for electronic and optoelectronic applications.

## 2. Result and Discussion

### 2.1. Synthesis and Crystal Structure of $SnSe_2$ Single Crystals

$SnSe_2$ crystallizes with a hexagonal space group $P$-3$m_1$ of the $CdI_2$-type, which consists of the $SnSe_6$ octahedral layers bonded together by weak van der Waal's forces to form 1T structure but an anisotropic atomic structure shown in **Figure 1**a. The single crystals SnSe2 bulk with the definite metallic sheen shown in Figure 1c have been synthesized by the direct transport method without transport gas (Figure 1b and Figure S2, Supporting Information), which have been confirmed by the powder X-ray diffraction (XRD; Figure S3, Supporting Information) and the energy dispersive X-ray (EDX) spectroscope with the formula of $SnSe_{1.96(2)}$ (Figure 1d), consistent with the calculation formula $SnSe_2$. The atomic structure of our $SnSe_2$ is also confirmed by the atomically resolved annual dark-field (ADF) scanning transmission electron microscopy (STEM), as shown in **Figure 2** and Figure S4 (Supporting Information). $SnSe_2$ flakes have been mechanically exfoliated from bulk single crystals onto the $SiO_2$/Si (285 nm thick $SiO_2$) substrate using the scotch tape and then transferred to TEM grids. Figure 2a displayed the film dominated by bilayered $SnSe_2$. The inset is the fast Fourier transform (FFT) pattern which shows sixfold-symmetric spots, indicating the hexagonal structure of the samples. Monolayer $SnSe_2$ can also be observed at some locations, which is indicated by a white rectangle in Figure 2a. This same region is presented in Figure 2b, where we can clearly identify the sites of Sn and In atoms. The Sn—Sn bond length is estimated to be ≈0.37 nm. This value fits to the simulation and model very well in Figure 2c,d.

### 2.2. AFM and Raman Spectra of Atomically Thick $SnSe_2$ Flakes

**Figure 3**a shows monolayer $SnSe_2$ with lateral dimensions exceeding 13 μm. Similar to other 2D atomic layers, the

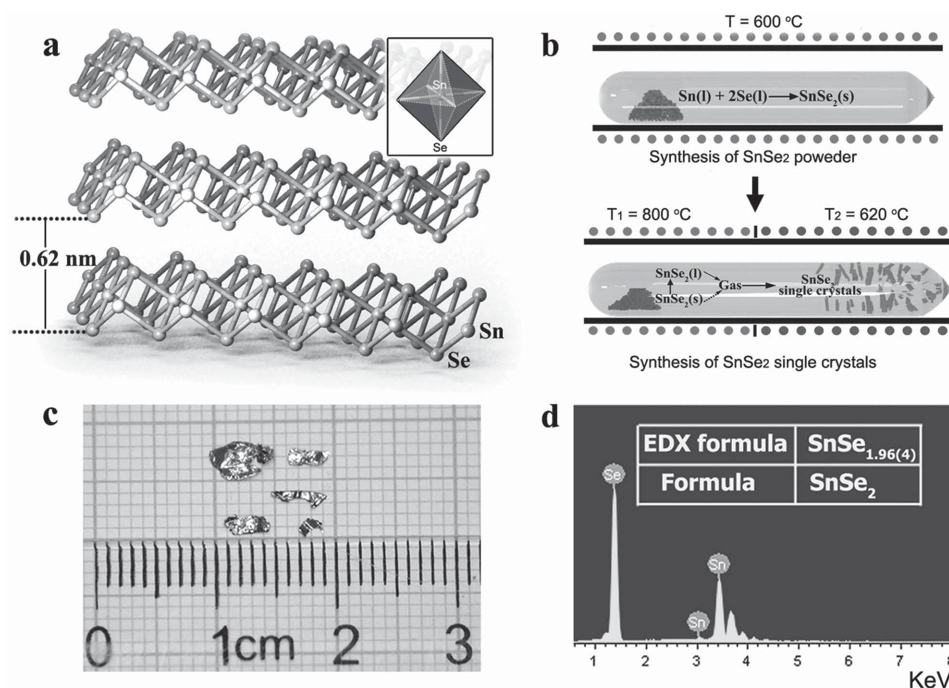


**Figure 1.** Synthesis and morphologies of $SnSe_2$ bulk single crystals. a) The structure of $SnSe_2$ with 0.62 nm of the thickness of monolayer, inset: $SnSe_6$ octahedron. b) The synthesis process of $SnSe_2$ polycrystalline powder (up) and the growth process of $SnSe_2$ single crystals using the vapor mass transport (VMT) technique without transport gas (down). c) The optical image of $SnSe_2$ single crystals with the size of several millimeters. d) EDX result of $SnSe_2$ single crystal.


© 2015 WILEY-VCH Verlag GmbH & Co. KGaA, Weinheim

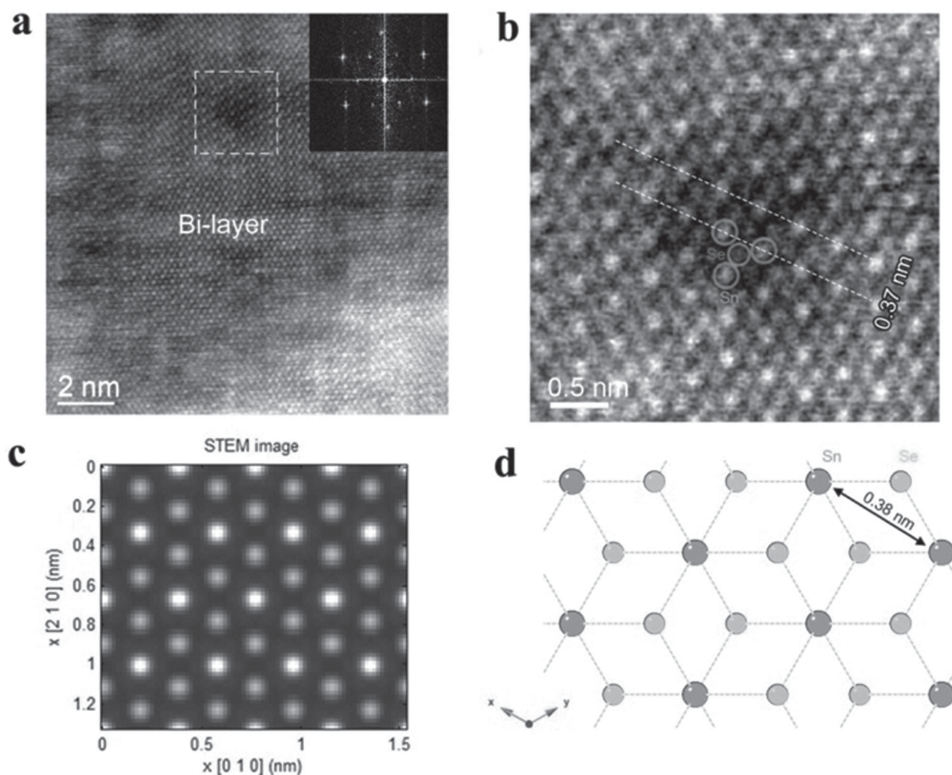


**Figure 2.** Atomically resolved imaging of few layered $SnSe_2$. a) $SnSe_2$ film dominated by bilayered $SnSe_2$. A small area of monolayer $SnSe_2$ is highlighted by the white rectangle. The inset is the corresponding fast Fourier transform (FFT) pattern. b) A closeup of the monolayer area. The Sn—Sn bond with 0.37 nm, which fits to the crystal model in (c,d) very well.

thickness of $SnSe_2$ layer can be roughly determined via the contrast of its optical images. In order to identify exactly the number of layers, AFM images are obtained from dashed-line region in Figure 3a. From the AFM images shown in Figure 3c, monolayer $SnSe_2$ is found along the edge with a thickness of ≈0.87 nm. It is slightly more than the actual thickness of 0.62 nm (Figure 1a) likely due to the trapping of absorbed molecular (e.g., $H_2O$) between the flake and the substrate and the measuring error of AFM, similar to the thickness variations in monolayer $SnS_2$ (1.0 ± 0.2 nm versus 0.6 nm).[32] In addition, the thickness of 2L, 3L, 4L, and 5L $SnSe_2$ is 1.48, 2.13, 2.69, and 3.36 nm, respectively, shown in Figure S5 (Supporting Information), which are also lightly more than the theoretical values, 1.24, 1.86, 2.48, and 3.1 nm. Therefore, the distances between 1L and 2L, 2L and 3L, and 4L and 5L are 0.61, 0.65, 0.56, and 0.67 nm, which is basically in accordance with the thickness of monolayer, 0.67 nm.

Raman spectroscopy is a powerful nondestructive characterization tool to confirm the phase of 2D crystals. The Raman spectrum of bulk 1T $SnSe_2$ has been reported by the previous papers, indicating that there were two vibratory modes $E_g$ (in-plane vibration) and $A_{1g}$ (out-plane vibration) with the values of 116.0 and 185.5 $cm^{-1}$ in 300 K excited by the 488 nm laser,[33] basically in accord with our experimental values of 110.6 and 183.5 $cm^{-1}$, respectively, under the 532 nm laser shown in Figure 3d and Figure S6 (Supporting Information), in which there is an obvious red shift for $A_{1g}$ with the reduction of the layer number but no change for $E_g$, compared to the change of Raman spectra of $MoS_2$ (blue and red shifts for $E_{2g}$ and $A_{1g}$ with reducing the layer number).[34] Moreover, the Raman map of the blue line region of the optical microscopy image displays the monolayer $SnSe_2$ is easily identified from different layer sample, shown in Figure 3b. The $A_{1g}$ mode shows low intensity in monolayer but is still detectable and can be clearly distinguished from bulk to monolayer $SnSe_2$ (Figure 3d). A plot of the intensity ratio of I(Si) and I($SnSe_2$) for the $A_{1g}$ and $E_g$ modes, respectively, with the function of the number of the layers is shown in Figure 3e. For the $A_{1g}$ mode, the I(Si)/I($SnSe_2$) intensity ratio of monolayer and bilayer is basically the same, and then decreases approximately linearly with the thickness. But for the $E_g$ mode, the I(Si)/I($SnSe_2$) intensity ratio always decreases approximately linearly with increasing the thickness. Therefore, the variation of the I(Si)/I($SnSe_2$) intensity ratio is basically normal.

### 2.3. Theoretical Calculations

The electronic band structures of bulk (**Figure 4**b), 4L (Figure S7b, Supporting Information), 3L (Figure S7a, Supporting Information), 2L (Figure 4c), and 1L (Figure 4d) have been obtained by the first-principles calculation based on density functional theory, respectively. Figure 4b shows bulk $SnSe_2$ are a semiconductor with an indirect bandgap of 0.710 eV, which is lower than the experimental value of 1.0 eV due to the insufficient cancellation of the self-interaction error by the


© 2015 WILEY-VCH Verlag GmbH & Co. KGaA, Weinheim

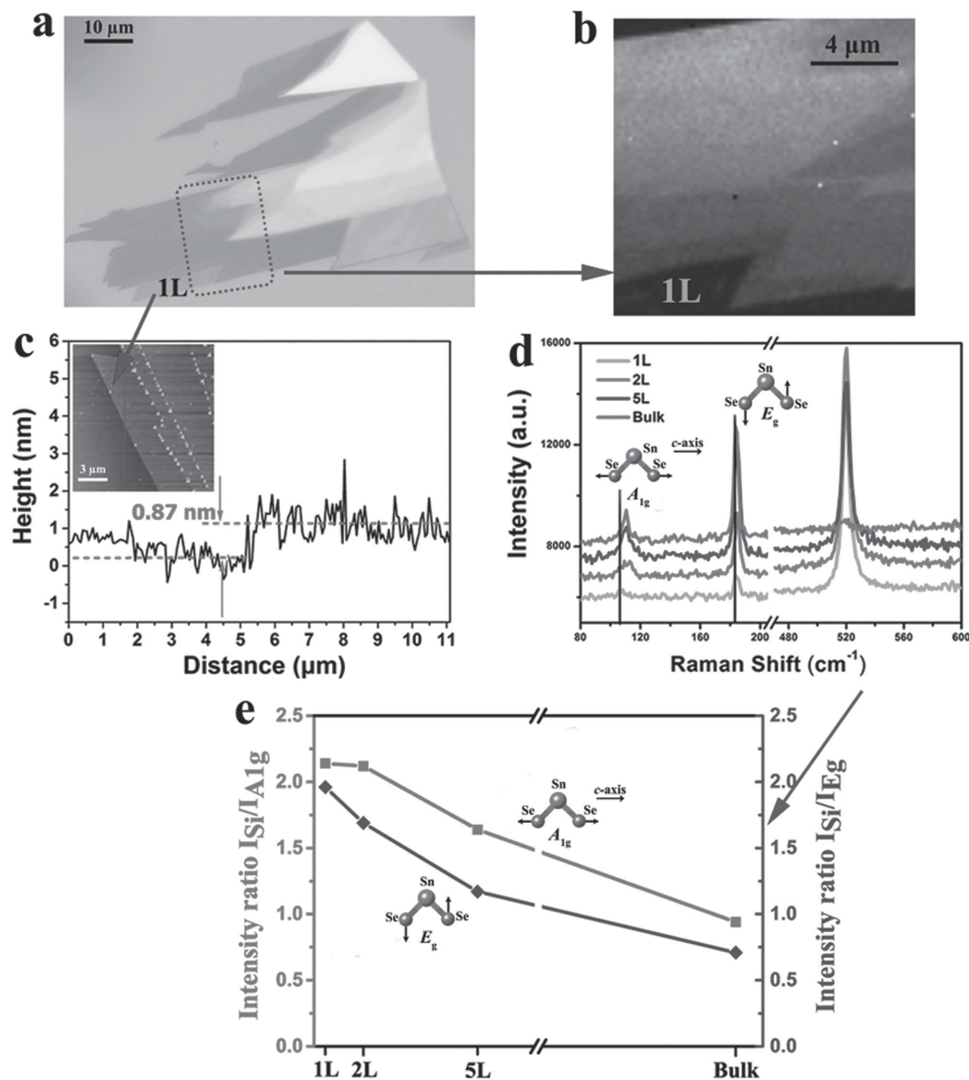


**Figure 3.** The characterization of few-layer and monolayer $SnSe_2$. a) Optical image of $SnSe_2$ flake placed on the surface of a silicon wafer capped by 285 nm thick silicon dioxide. b) Raman mapping image of the blue region in (a), which clearly displays the monolayer. c) The thickness of monolayer $SnSe_2$, inset: AFM image of the different thick sample. d) Normalized Raman spectra of $SnSe_2$ from monolayer to bulk. The intensity of Si peak is set as constant. e) The Raman intensity ratio of Si/$A_{1g}$ and Si/$E_g$ with the dependence of the various thick layers. The insets in (d) and (e) are the schematics of displacement of atom for Raman active $A_{1g}$ and $E_g$ modes in $SnSe_2$.

approximate generalized gradient approximation (GGA) functionals.[35] Of particular interest of our finding from the band structure is that the bandgap is insensitive on the number of layers compared with the observations in $MoS_2$ and black phosphorus.[18,36] In addition, the calculated results show $SnSe_2$ from bulk to monolayer always have the indirect bandgaps, which have been confirmed by the photoluminescent measurement with no photoluminescent (PL) phenomenon from bulk to monolayer, which is different from $MoS_2$ which has an indirect bandgap for bulk but a direct bandgap for monolayer.[18]

### 2.4. The Electronic Properties of Bilayered $SnSe_2$ FET

The electrical contacts made of Ti/Au films have been deposited by an e-beam evaporator after photolithography, shown in **Figure 5**a. The substrate and the electrode are attached to chip carrier fixtures for electrical testing. The current–voltage ($I_d$–$V_d$) curve and the transfer characteristics ($I_d$–$V_g$) of the fabricated $SnSe_2$ transistor in the absence of laser irradiation are shown in Figure 5b,c. It can be depicted that the bilayer $SnSe_2$ FET exhibited n-type semiconducting behavior, which is consistent with theoretical results and previous literatures.[29] On the other hand, we also observe a clear hysteresis loop in the electrical characteristics, resulting from surrounding conditions or the charge transfer from neighboring adsorbates or trapping states on the substrate.[37] The mobility of the carriers can be calculated by $\mu = \frac{L}{W \times (\varepsilon_0 \varepsilon_r / d)} \times \frac{dI_{ds}}{dV_G} \times \frac{1}{V_{ds}}$, where $L$, $W$, and $d$ denote the channel length, width, and thickness of $SiO_2$ layer (285 nm in our devices), respectively. $V_{ds}$, $I_{ds}$, and $V_b$ denote the source–drain bias, current, and bottom gate voltage in the linear region in the $I_d$–$V_g$ curve. $\varepsilon_0$ and $\varepsilon_r$ are the vacuum dielectric constant


© 2015 WILEY-VCH Verlag GmbH & Co. KGaA, Weinheim

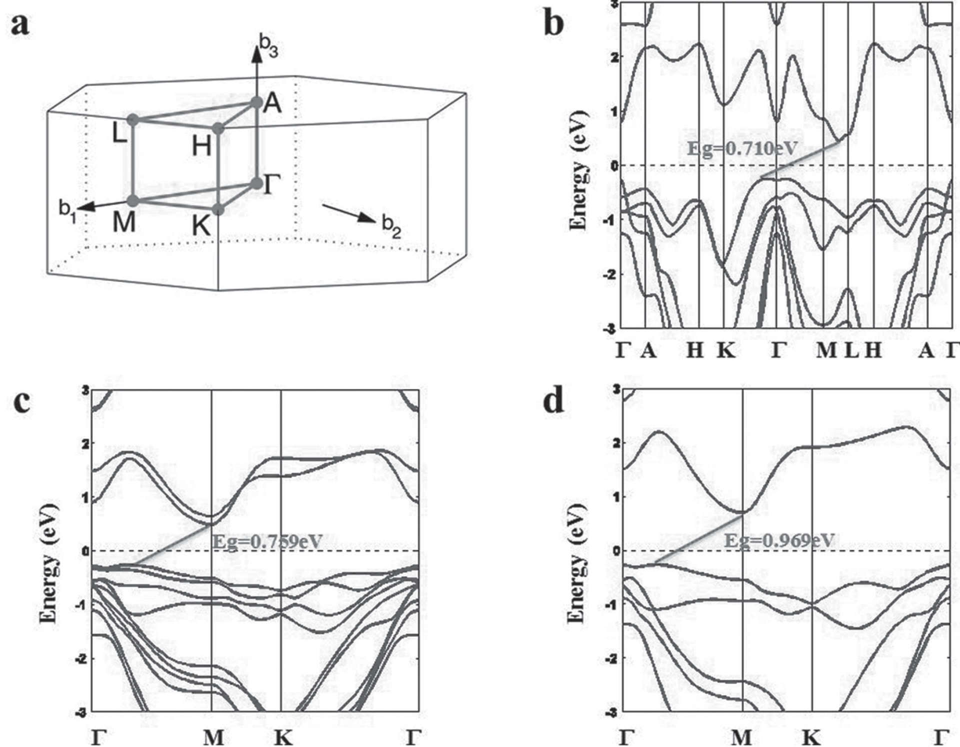


**Figure 4.** The calculated electronic band structures of $SnSe_2$ with the spin–orbit couple (SOC) from bulk to monolayer. a) The Brillouin zone of $SnSe_2$. The band structures of b) bulk, c) bilayer, and d) monolayer. The indirect bandgaps of bulk, bilayer, and monolayer $SnSe_2$ are 0.710, 0.759, and 0.969 eV, respectively.

and the dielectric constant of $SiO_2$ ($\varepsilon_r$ = 3.9), respectively. The calculated mobility of our device is about 4 $cm^2 V^{-1} s^{-1}$, which is at least one order higher than that of other similar compounds such as GaS, GaSe, GaTe, and $WS_2$,[16,38] even though it is much lower than these of $MoS_2$ and $WSe_2$.[39,40] Furthermore, the mobility can be improved by optimizing crystal quality, contact resistance, and the dielectric environment similar to $MoS_2$ transistors, the mobility of which is increased from 0.1 $cm^2 V^{-1} s^{-1}$ to nearly 200 $cm^2 V^{-1} s^{-1}$ by employing high-*k* gating of $HfO_2$ layer.[41] The relatively high mobility of the $SnSe_2$ transistor could be applied in optoelectronic and photonic applications. Figure 5c,d displays the on/off ratio of FET fabricated by bilayer $SnSe_2$ is up to $10^3$, compared with single digit ratio reported 84 nm thick SnSe2 based FET.[29] In the dark state, our device shows a typical behavior of n-type transistor and a threshold voltage of $V_t$ = 5 V. When we illuminated the biased device using a focused 633 nm laser, the dark current increased in the range of 10 nA. As a result, the photocurrent dominates over the tunneling currents and thermionic currents in the operating working range, indicating that the $SnSe_2$ FET is suitable for photodetector device.

### 2.5. The Optoelectronic Properties of Bilayered $SnSe_2$ Photodetector

We probed the bilayer $SnSe_2$ FET devices (**Figure 6**a,b) and their time-dependent photoresponse to laser excitation using a focused laser beam ($\lambda$ = 633 nm) and an illumination power of 4 mW. A parabolic mirror and a micromechanical stage were used to localize the device. The spot size has a typical diameter of ≈0.5 mm, resulting in an estimated maximum illumination intensity of ≈0.64 W $cm^{-2}$. The time-dependent photocurrent measurement results are shown in Figure 6c,d. The photocurrent $I_{ph}$ ($I_{ph} = I_{illuminated} - I_{dark}$) of $SnSe_2$ FET is about $10^5$ nA corresponding to a photoresponsivity of ≈0.5 A $W^{-1}$ under a source–drain bias of 100 mV. The photocurrent can be further increased by applying a higher source–drain voltage, as shown in Figure 6d. The decay time can be fitted by the following equation: $I_{rise} = I_0 - A\exp(-(t-t_1)/\tau_1)$ and $I_{decay} = I_0 + B\exp(-(t-t_2)/\tau_2)$,[42] where $\tau$ is the time constant and $t$ is the time when laser is switched on or off. $I_{dark}$ is the dark current and $A$ is the scaling constant. The fitted characteristic photoresponse time coefficients, $\tau_1$ and $\tau_2$, are 2.2 ± 0.3 ms (rise) and 3.2 ± 0.2 ms (fall), respectively, which is one of the fastest response times among all types of 2D photodetectors, e.g., 600 ms for 1L $MoS_2$,[43] 5.3 ms for few-layered $WS_2$,[44] 6 ms for multilayer GaTe,[16] 20 ms for multilayer GaSe,[45] etc. On the other hand, the rise time and fall time can also be calculated by the time period between 10% and 90% of the current in the arising and falling curves, as shown in Figure 6c. The rise time ($\tau_1$ = 2.1 ms) and fall time ($\tau_2$ = 3.2 ms) are consistent with the former fitted values. Further improvement of the mobility by dielectric engineering or decreasing the thickness of the $SnSe_2$ layer may further boost the response time. More importantly, due to the phase changing property of $SnSe_2$, the


© 2015 WILEY-VCH Verlag GmbH & Co. KGaA, Weinheim

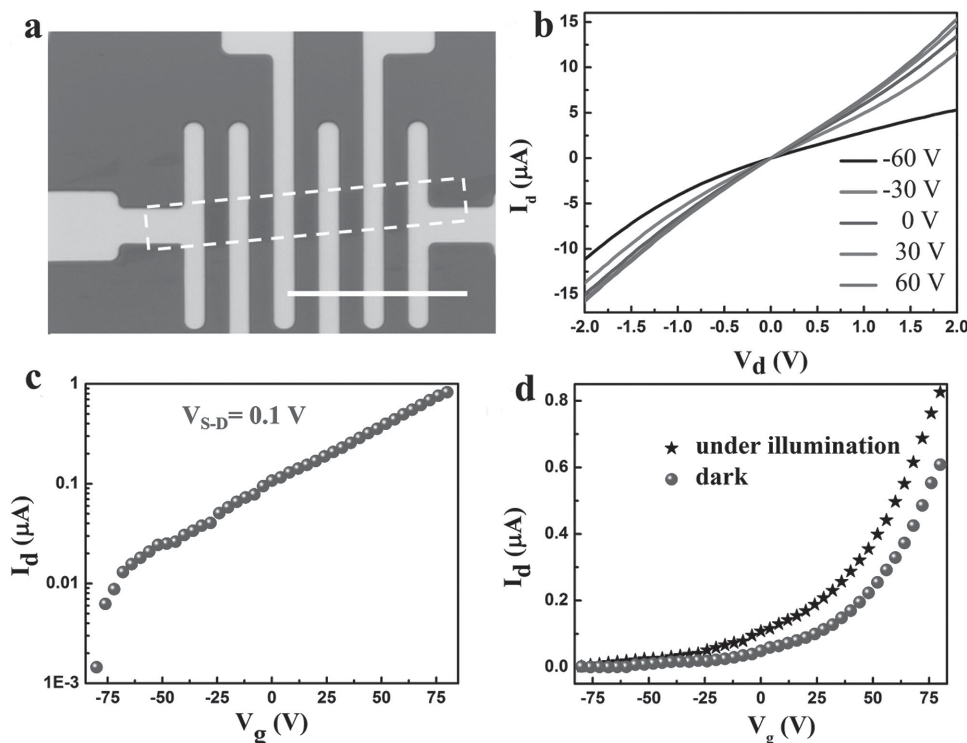


**Figure 5.** The electrical property of the fabricated $SnSe_2$ bilayer FET. a) Optical microscopy image of a bilayer SnSe2 FET device with Ti/Au as the electrodes on $Si/SiO_2$ substrate. The scale bar is 20 μm. The white-color dashed line indicates the sample area. b) Current–voltage ($I_d$–$V_d$) curve acquired with different gate voltages (without light illumination). c) Gating response ($I_d$–$V_g$) of the $SnSe_2$ FET acquired for a backgate voltage $V_g$ between −80 V and 80 V with a source–drain voltage ($V_{S-D}$) of 0.1 V (without light illumination). d) Gating response ($I_d$–$V_g$) of the $SnSe_2$ transistor in dark and illuminated states. The illumination intensity is 500 W cm$^2$.

performance of the $SnSe_2$ photodetector can be improved by phase engineering analogous to $MoS_2$.[46]

On the other hand, with increasing laser power, the photoresponse can be expressed by a power law $I_{PC} = CP\gamma$ ($C$ is a constant and $P$ is the illumination power) as shown in Figure 6e. For the laser with the wavelength of 532 and 633 nm, $\gamma$ is 0.90 and 0.82, respectively, indicating that the recombination kinetics of photocarriers involves both traps states and interactions between photogenerated carriers. The decrease of the photocurrent with the incident laser power can be attributed to the reduction of the numbers of photogenerated carriers available for extraction under high photon flux due to the Auger process or the saturation of recombination/trap states that influence the lifetime of the generated carriers.[47,48] The Schottky junction formed at the metal–$SnSe_2$ interfaces is also important to the photocurrent generation, which can be inferred from Figure 6f that a nonlinear effect is observed in the photocurrent generation with various bias voltage. Considering the tradeoff between response time and responsivity for typical materials used in photodetectors, our $SnSe_2$-based photodetector shows a relatively faster response time compared to other 2D metal chalcogenides, but slower than that of graphene photodetector which has an ultrahigh mobility. The responsivity of $SnSe_2$-based photodetector is higher than these of graphene,[49] $WS_2$,[44] and $WSe_2$,[50] but still lower than these of $MoS_2$[43,51] and GaTe,[16] which might be attributed to the lower light absorption efficiency and higher carriers scattering in $SnSe_2$ in the semiconductor channel.

## 3. Conclusion

The properties of few-layer and monolayer $SnSe_2$, a new 2D material whose components are both cheap and earth-abundant, have been first investigated systematically in this paper using comprehensive characterization, device fabrication, and measurement of electronic and optoelectronic device. We unambiguously identify monolayer and few-layer $SnSe_2$ by optical and AFM, whose monolayer thickness is ≈0.87 nm. Moreover, combined with AFM, Raman spectra of monolayer and few-layer $SnSe_2$ have been studied, which show an obvious red shift for $A_{1g}$ with the reduction of the layer number but no change for $E_g$. Electronic structure calculations indicate the bandgap is indirect from bulk to monolayer, consistent with the behavior observed in $SnS_2$ and contrast with $MoS_2$. We have successfully fabricated back-gated electronic and optoelectronic device based on bilayer $SnSe_2$ with thermal evaporated $SiO_2$ as dielectric layer, which exhibit a mobility of up to 4 cm$^2$ V$^{-1}$ s$^{-1}$ and an on/off ratio of $10^3$ at room temperature and the dark state. Moreover, the bilayer SnSe2 photodetector upon illumination of 633 nm laser displays a good responsivity of 0.5 A W$^{-1}$ and a very fast time response of 2.2 ± 0.3 ms (rise) and 3.2 ± 0.2 ms (fall), which


© 2015 WILEY-VCH Verlag GmbH & Co. KGaA, Weinheim

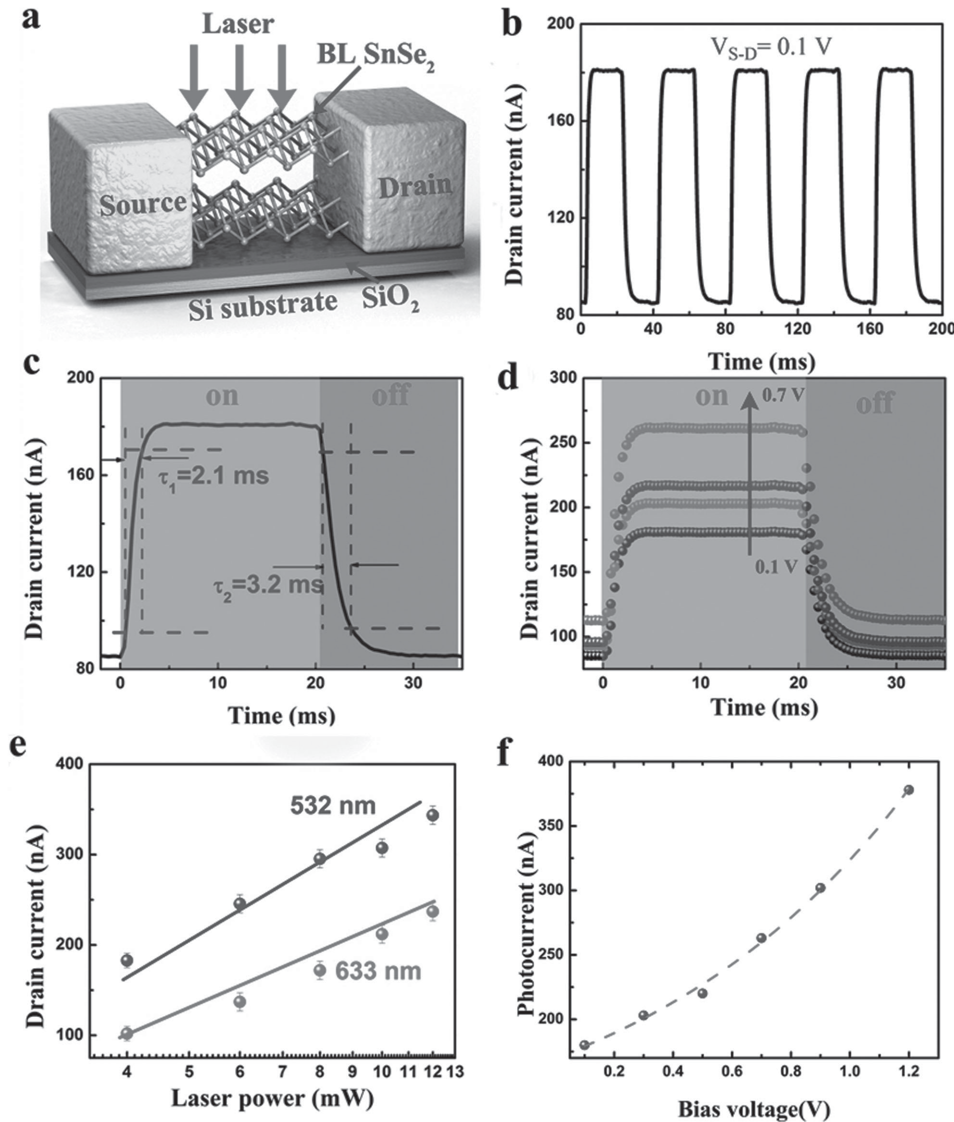


**Figure 6.** The optoelectronic properties of the fabricated $SnSe_2$ bilayer device. a) Schematic representation of the photodetector device consisting of a bilayered $SnSe_2$ on $SiO_2$/Si wafer with laser illumination. b) Time-resolved photoresponse of the device recorded for a bias voltage of 0.1 V and zero gate voltage. c) Photocurrent dynamics of one period of the time-resolved photoresponse. The laser used in (b) and (c) is 633 nm with a power of 4 mW. d) Time-resolved photoresponse of the device recorded for different source–drain voltages varying from 0.1 to 0.7 V at a step of 0.2 V with 633 nm laser illumination (4 mW). e) Power dependences of the photocurrent with 532 and 633 nm laser illumination recorded at $V_{SD}$ = 0.1 V. f) Photocurrent response-bias characteristic of the device under 632 nm laser illumination with a power of 4 mW.

make it also a promising 2D material for photodetection in the visible region.

## 4. Experimental Section

*Synthesis and Mechanical Exfoliation of $SnSe_2$ Single Crystals*: Polycrystalline $SnSe_2$ was prepared by melting stoichiometric amounts of Sn powder (99.99%, Sigma-Aldrich) and Se powder (99.995%, Sigma-Aldrich), which were sealed in an evacuated quartz ampoule under vacuum at $10^{-6}$ Torr and then placed in one-zone tube furnace with the heating procedure: heated to 600 °C in 10 h, dwelt for 24 h, then naturally cooled to room temperature. The obtained sample, which is in the form of a shining polycrystalline mass, was the pure phase of $SnSe_2$ confirmed by powder XRD (Figure S3, Supporting Information). In order to obtain the high quality single crystals of $SnSe_2$, a direct transport method without the transport gas was applied due to the good volatility of $SnSe_2$ in vacuum. Prior to the growth of the single crystals, the $SnSe_2$ polycrystalline sample was grinded to the powder in a mortar and then sealed in a 23 cm long quartz tube under vacuum $10^{-6}$ Torr. The quartz tube was placed in a two-zone furnace with the reaction zone at a higher temperature of 800 °C and the growth zone at a lower temperature of 620 °C for 3 d. In this method, the shining black opaque single crystals of $SnSe_2$ were obtained in the growth zone (Figure 1c). Monolayer and few-layer $SnSe_2$ flakes were mechanically exfoliated from bulk $SnSe_2$ single crystals and transferred to a silicon substrate with a 285 nm thick silica layer using the scotch tape-based mechanical exfoliation method, which was widely employed for the preparation of monolayer graphene and transitional metal dichalcogenides (TMDs).

*Elemental Analysis*: Semi-quantitative microprobe analyses on the single crystals of $SnSe_2$ were performed with the aid of a field emission


© 2015 WILEY-VCH Verlag GmbH & Co. KGaA, Weinheim

scanning electron microscope (JSM-5410) equipped with an EDX spectroscope (Oxford INCA). The energy dispersive spectra taken on visibly clean surfaces of the sample proved the presence of Sn and Se with the formula $SnSe_{1.96(2)}$ shown in Figure 1d.

*Powder X-Ray Diffraction*: The powder XRD patterns were collected using a Rigaku DMAX 2500 diffractometer with monochromatized Cu-K$\alpha$ radiation at room temperature in the $2\theta$ range of 10°–85° with a scan step width of 0.05°. The measured X-ray powder diffraction patterns were in accordance with the calculated ones simulated from the single crystal data as shown in Figure S3 (Supporting Information).

*TEM Sample Preparations and AD-STEM Imaging and Image Simulations*: The TEM sample was prepared by transferring the $SnSe_2$ flakes onto lacey-carbon grid after evaporating a drop of isopropanol alcohol (IPA) solvent and etching away the underneath $SiO_2$ layer with potassium hydroxide solution. The as-prepared TEM membranes were briefly irradiated in TEM mode before ADF-STEM characterization. The ADF-STEM was done with an FEI Titan ChemiSTEM equipped with a probe corrector. This microscope was operated with an acceleration voltage of 80 kV. The convergent angle for illumination was about 22 mrad with a probe current of 70 pA, and the collection angle was about 43.4–200 mrad. ADF-STEM image simulations of pristine $SnSe_2$ were done with software STEMSIM.[52] The input parameters were set according to the experimental conditions: collection angle was about 45–200 mrad, acceleration voltage and C3 were 80 kV and 1.5 µm, respectively. A Wiener and average background subtracted filter was applied to Figure 2a,d, based on R. Kilaas's work and developed by David Mitchell.

*Thickness Measurements*: The thickness measurements of monolayer and few-layer were carried out in atomic force microscopy (DI-3100), which shows the thickness of monolayer $SnSe_2$ is 0.87 nm shown in Figure 3c.

*Raman Spectra*: Analysis of atomically thin $SnSe_2$ flakes and bulk sample by Raman spectroscopy was carried out on a WITec CRM200 confocal Raman microscopy system with the excitation line of 532 nm and an air-cooling charge-coupled device as the detector (WITec Instruments Corp, Germany).

*Calculations of Band Structure of $SnSe_2$ from Bulk to Monolayer*: The first-principles calculations were based on the GGA[53] using the projector augmented wave method[54,55] as implemented in the Vienna ab initio simulation (VASP) package.[56,57] The kinetic energy cutoff of 500 eV was used, and the spin–orbit coupling was included in all the calculations. A vacuum layer of 15 Å was adopted to avoid interactions between neighboring layers for slab calculations. The numerical integration of the Brillouin zone was performed based on an $8 \times 8 \times 6$ $k$-point mesh-grid for 3D bulk $SnSe_2$ and an $8 \times 8 \times 1$ $k$-point mesh-grid for 2D $SnSe_2$.

*The Fabrication and Measurements of the Devices*: The devices were fabricated by standard optical lithography and deposited Ti/Au (20 nm/80 nm) as contact electrodes using electron-beam evaporation. The final devices were annealed at 400 K for 2 h with the protection of nitrogen in order to remove resist residues and enhance the metallic contacts. Electrical characterization was performed by current–voltage measurements on a probe station using a semiconductor characterization system (Agilent, B1500A). Furthermore, the phototransistor performance was measured using a 633 nm laser.

## Supporting Information

Supporting Information is available from the Wiley Online Library or from the author.

## Acknowledgements

P.Y., X.Y., and W.L. contributed equally to this work. This work was supported by the National Research Foundation Singapore under NRF RF Award No. NRF-RF2013-08. This work was also supported by MOE2011-T2-2-147 and MOE2011-T3-1-005 from the Ministry of Education, Singapore. Part of the electron microscopy characterizations was carried out at the Center for Electron Microscopy of Zhejiang University. W.L. and C.J. acknowledge financial support by the National Basic Research Program of China (2014CB932500 and 2015CB921000), the National Science Foundation of China (51222202, 51410305074, and 51472215), the Program for Innovative Research Team in University of Ministry of Education of China (IRT13037), and the Fundamental Research Funds for the Central Universities (2014XZZX003-07). H.L. acknowledges the Singapore National Research Foundation for the support under NRF Award No. NRF-NRFF2013-03.

Received: September 7, 2015
Revised: October 8, 2015
Published online: November 19, 2015

[1] K. S. Novoselov, A. K. Geim, S. V. Morozov, D. Jiang, Y. Zhang, S. V. Dubonos, I. V. Grigorieva, A. A. Firsov, *Science* **2004**, *306*, 666.
[2] Y. B. Zhang, Y. W. Tan, H. L. Stormer, P. Kim, *Nature* **2005**, *438*, 201.
[3] K. S. Novoselov, A. K. Geim, S. V. Morozov, D. Jiang, M. I. Katsnelson, I. V. Grigorieva, S. V. Dubonos, A. A. Firsov, *Nature* **2005**, *438*, 197.
[4] A. Rycerz, J. Tworzydlo, C. W. J. Beenakker, *Nat. Phys.* **2007**, *3*, 172.
[5] M. Corso, W. Auwarter, M. Muntwiler, A. Tamai, T. Greber, J. Osterwalder, *Science* **2004**, *303*, 217.
[6] L. Song, L. J. Ci, H. Lu, P. B. Sorokin, C. H. Jin, J. Ni, A. G. Kvashnin, D. G. Kvashnin, J. Lou, B. I. Yakobson, P. M. Ajayan, *Nano Lett.* **2010**, *10*, 3209.
[7] Z. Liu, L. L. Ma, G. Shi, W. Zhou, Y. J. Gong, S. D. Lei, X. B. Yang, J. N. Zhang, J. J. Yu, K. P. Hackenberg, A. Babakhani, J. C. Idrobo, R. Vajtai, J. Lou, P. M. Ajayan, *Nat. Nanotechnol.* **2013**, *8*, 119.
[8] E. Rokuta, Y. Hasegawa, K. Suzuki, Y. Gamou, C. Oshima, A. Nagashima, *Phys. Rev. Lett.* **1997**, *79*, 4609.
[9] S. Najmaei, Z. Liu, W. Zhou, X. L. Zou, G. Shi, S. D. Lei, B. I. Yakobson, J. C. Idrobo, P. M. Ajayan, J. Lou, *Nat. Mater.* **2013**, *12*, 754.
[10] K. F. Mak, K. L. He, J. Shan, T. F. Heinz, *Nat. Nanotechnol.* **2012**, *7*, 494.
[11] Q. Q. Ji, Y. F. Zhang, T. Gao, Y. Zhang, D. L. Ma, M. X. Liu, Y. B. Chen, X. F. Qiao, P. H. Tan, M. Kan, J. Feng, Q. Sun, Z. F. Liu, *Nano Lett.* **2013**, *13*, 3870.
[12] Y. Zhang, T. R. Chang, B. Zhou, Y. T. Cui, H. Yan, Z. K. Liu, F. Schmitt, J. Lee, R. Moore, Y. L. Chen, H. Lin, H. T. Jeng, S. K. Mo, Z. Hussain, A. Bansil, Z. X. Shen, *Nat. Nanotechnol.* **2014**, *9*, 111.
[13] X. Lu, M. I. B. Utama, J. H. Lin, X. Gong, J. Zhang, Y. Y. Zhao, S. T. Pantelides, J. X. Wang, Z. L. Dong, Z. Liu, W. Zhou, Q. H. Xiong, *Nano Lett.* **2014**, *14*, 2419.
[14] Y. F. Lin, Y. Xu, S. T. Wang, S. L. Li, M. Yamamoto, A. Aparecido-Ferreira, W. W. Li, H. B. Sun, S. Nakaharai, W. B. Jian, K. Ueno, K. Tsukagoshi, *Adv. Mater.* **2014**, *26*, 3263.
[15] W. Liu, J. H. Kang, D. Sarkar, Y. Khatami, D. Jena, K Banerjee, *Nano Lett.* **2013**, *13*, 1983.
[16] F. C. Liu, H. Shimotani, H. Shang, T. Kanagasekaran, V. Zolyomi, N. Drummond, V. I. Fal'ko, K. Tanigaki, *ACS Nano* **2014**, *8*, 752.
[17] S. R. Tamalampudi, Y. Y. Lu, U. R. Kumar, R. Sankar, C. D. Liao, B. K. Moorthy, C. H. Cheng, F. C. Chou, Y. T. Chen, *Nano Lett.* **2014**, *14*, 2800.
[18] L. K. Li, Y. J. Yu, G. J. Ye, Q. Q. Ge, X. D. Ou, H. Wu, D. L. Feng, X. H. Chen, Y. B. Zhang, *Nat. Nanotechnol.* **2014**, *9*, 372.
[19] M. Chhowalla, G. A. J. Amaratunga, *Nature* **2000**, *407*, 164.
[20] J. Xiao, D. W. Choi, L. Cosimbescu, P. Koech, J. Liu, J. P. Lemmon, *Chem. Mater.* **2010**, *22*, 4522.


© 2015 WILEY-VCH Verlag GmbH & Co. KGaA, Weinheim

[21] Y. G. Li, H. L. Wang, L. M. Xie, Y. Y. Liang, G. S. Hong, H. J. Dai, *J. Am. Chem. Soc.* **2011**, *133*, 7296.
[22] Q. H. Wang, K. Kalantar-Zadeh, A. Kis, J. N. Coleman, M. S. Strano, *Nat. Nanotechnol.* **2012**, *7*, 699.
[23] V. Podzorov, M. E. Gershenson, C. Kloc, R. Zeis, E. Bucher, *Appl. Phys. Lett.* **2004**, *84*, 3301.
[24] T. Tani, T. Osada, S. Tanaka, *Solid State Commun.* **1977**, *22*, 269.
[25] J. A. Galvis, L. Chirolli, I. Guillamon, S. Vieira, E. Navarro-Moratalla, E. Coronado, H. Suderow, F. Guinea, *Phys. Rev. B* **2014**, *89*, 224512.
[26] A. D. Yoffe, *Chem. Soc. Rev.* **1976**, *5*, 51.
[27] D. Voiry, H. Yamaguchi, J. W. Li, R. Silva, D. C. B. Alves, T. Fujita, M. W. Chen, T. Asefa, V. B. Shenoy, G. Eda, M. Chhowalla, *Nat. Mater.* **2013**, *12*, 850.
[28] B. Mahler, V. Hoepfner, K. Liao, G. A. Ozin, *J. Am. Chem. Soc.* **2014**, *136*, 14121.
[29] Y. Su, M. A. Ebrish, E. J. Olson, S. J. Koester, *Appl. Phys. Lett.* **2013**, *103*, 263104.
[30] R. Y. Wang, M. A. Caldwell, R. G. D. Jeyasingh, S. Aloni, R. M. Shelby, H. S. P. Wong, D. J. Milliron, *J. Appl. Phys.* **2011**, *109*, 113506.
[31] T. S. Pan, D. De, J. Manongdo, A. M. Guloy, V. G. Hadjiev, Y. Lin, H. B. Peng, *Appl. Phys. Lett.* **2013**, *103*, 093108.
[32] Y. Huang, E. Sutter, J. T. Sadowski, M. Cotlet, O. L. A. Monti, D. A. Racke, M. R. Neupane, D. Wickramaratne, R. K. Lake, B. A. Parkinson, P. Sutter, *ACS Nano* **2014**, *8*, 10743.
[33] D. G. Mead, J. C. Irwin, *Solid State Commun.* **1976**, *20*, 885.
[34] H. Li, Q. Zhang, C. C. R. Yap, B. K. Tay, T. H. T. Edwin, A. Olivier, D. Baillargeat, *Adv. Funct. Mater.* **2012**, *22*, 1385.
[35] K. M. S. Etheredge, R. Mackay, G. L. Schimek, S. J. Hwu, *Inorg. Chem.* **1996**, *35*, 7919.
[36] K. F. Mak, C. Lee, J. Hone, J. Shan, T. F. Heinz, *Phys. Rev. Lett.* **2010**, *105*, 136805.
[37] H. M. Wang, Y. H. Wu, C. X. Cong, J. Zh. Shang, T. Yu, *ACS Nano* **2010**, *4*, 7221.
[38] D. J. Late, B. Liu, J. J. Luo, A. M. Yan, H. S. S. R. Matte, M. Grayson, C. N. R. Rao, V. P. Dravid, *Adv. Mater.* **2012**, *24*, 3549.
[39] X. Cui, G. H. Lee, Y. D. Kim, G. Arefe, P. Y. Huang, C. H. Lee, D. A. Chenet, X. Zhang, L. Wang, F. Ye, F. Pizzocchero, B. S. Jessen, K. Watanabe, T. Taniguchi, D. A. Muller, T. Low, P. Kim, J. Hone, *Nat. Nanotechnol.* **2015**, *10*, 534.
[40] H. J. Chuang, X. B. Tan, N. J. Ghimire, M. M. Perera, B. Chamlagain, M. M. C. Cheng, J. Q. Yan, D. Mandrus, D. Tomanek, Z. X. Zhou, *Nano Lett.* **2014**, *14*, 3594.
[41] B. Radisavljevic, A. Radenovic, J. Brivio, V. Giacometti, A. Kis, *Nat. Nanotechnol.* **2011**, *6*, 147.
[42] B. Chitara, L. S. Panchakarla, S. B. Krupanidhi, C. N. R. Rao, *Adv. Mater.* **2011**, *23*, 5419.
[43] O. Lopez-Sanchez, D. Lembke, M. Kayci, A. Radenovic, A. Kis, *Nat. Nanotechnol.* **2013**, *8*, 497.
[44] N. Perea-Lopez, A. L. Elias, A. Berkdemir, A. Castro-Beltran, H. R. Gutierrez, S. M. Feng, R. T. Lv, T. Hayashi, F. Lopez-Urias, S. Ghosh, B. Muchharla, S. Talapatra, H. Terrones, M. Terrones, *Adv. Funct. Mater.* **2013**, *23*, 5511.
[45] P. A. Hu, Z. Z. Wen, L. F. Wang, P. H. Tan, K. Xiao, *ACS Nano* **2012**, *6*, 5988.
[46] R. Kappera, D. Voiry, S. E. Yalcin, B. Branch, G. Gupta, A. D. Mohite, M. Chhowalla, *Nat. Mater.* **2014**, *13*, 1128.
[47] Z. H. Sun, Z. K. Liu, J. H. Li, G. A. Tai, S. P. Lau, F. Yan, *Adv. Mater.* **2012**, *24*, 5878.
[48] G. Konstantatos, M. Badioli, L. Gaudreau, J. Osmond, M. Bernechea, F. P. G. de Arquer, F. Gatti, F. H. L. Koppens, *Nat. Nanotechnol.* **2012**, *7*, 363.
[49] M. C. Lemme, F. H. L. Koppens, A. L. Falk, M. S. Rudner, H. Park, L. S. Levitov, C. M. Marcus, *Nano Lett.* **2011**, *11*, 4134.
[50] D. J. Groenendijk, M. Buscema, G. A. Steele, S. M. de Vasconcellos, R. Bratschitsch, H. S. J. van der Zant, A. Castellanos-Gomez, *Nano Lett.* **2014**, *14*, 5846.
[51] Z. Y. Yin, H. Li, H. Li, L. Jiang, Y. M. Shi, Y. H. Sun, G. Lu, Q. Zhang, X. D. Chen, H. Zhang, *ACS Nano* **2012**, *6*, 74.
[52] A. Rosenauer, M. Schowalyer, *Microscopy of Semiconducting Materials*, Springer, Netherlands **2007**, p. 170.
[53] J. P. Perdew, K. Burke, M. Ernzerhof, *Phys. Rev. Lett.* **1996**, *77*, 3865.
[54] P. E. Blochl, *Phys. Rev. B* **1994**, *50*, 17953.
[55] G. Kresse, D. Joubert, *Phys. Rev. B* **1999**, *59*, 1758.
[56] G. Kresse, J. Hafner, *Phys. Rev. B* **1993**, *48*, 13115.
[57] G. Kresse, J. Furthmuller, *Phys. Rev. B* **1996**, *54*, 11169.


© 2015 WILEY-VCH Verlag GmbH & Co. KGaA, Weinheim